

# Journal Pre-proof

Microscopic insights on the degradation of a PEM water electrolyzer with ultra-low catalyst loading

Haoran Yu, Leonard Bonville, Jasna Jankovic, Radenka Maric



PII: S0926-3373(19)30941-5  
DOI: <https://doi.org/10.1016/j.apcatb.2019.118194>  
Reference: APCATB 118194

To appear in: *Applied Catalysis B: Environmental*

Received Date: 6 July 2019  
Revised Date: 12 September 2019  
Accepted Date: 13 September 2019

Please cite this article as: Yu H, Bonville L, Jankovic J, Maric R, Microscopic insights on the degradation of a PEM water electrolyzer with ultra-low catalyst loading, *Applied Catalysis B: Environmental* (2019), doi: <https://doi.org/10.1016/j.apcatb.2019.118194>

This is a PDF file of an article that has undergone enhancements after acceptance, such as the addition of a cover page and metadata, and formatting for readability, but it is not yet the definitive version of record. This version will undergo additional copyediting, typesetting and review before it is published in its final form, but we are providing this version to give early visibility of the article. Please note that, during the production process, errors may be discovered which could affect the content, and all legal disclaimers that apply to the journal pertain.

© 2019 Published by Elsevier.

# Microscopic insights on the degradation of a PEM water electrolyzer with ultra-low catalyst loading

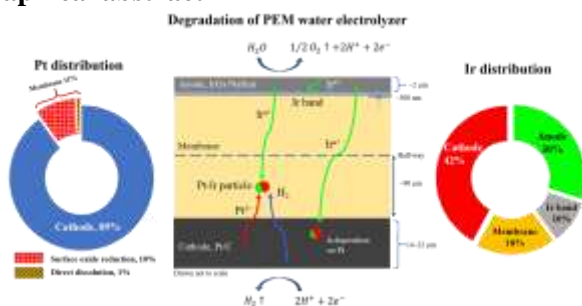
Haoran Yu<sup>1,2</sup>, Leonard Bonville<sup>2</sup>, Jasna Jankovic<sup>2,3</sup>, Radenka Maric<sup>1,2,3</sup>

<sup>1</sup>Department of Chemical and Biomolecular Engineering, University of Connecticut, 191 Auditorium Road, Unit 3222, Storrs, CT 06269-3222, USA

<sup>2</sup>Center for Clean Energy Engineering, University of Connecticut, 44 Weaver Road Unit 5233, Storrs, CT, 06269-5223, USA

<sup>3</sup>Department of Material Science and Engineering, University of Connecticut, 97 North Eagleville Road, Storrs, CT, 06269-3136, USA

## Graphical abstract



## Highlights

- Comprehensive study of degraded PEM water electrolyzer after 4500h operation.
- Ultra-low catalyst loaded membrane electrode assembly (MEA) was analyzed.
- Cathode degradation was proposed based on established physical models.
- The distribution of Pt and Ir in degraded MEA was quantified.

## Abstract

The present work aims for a comprehensive understanding of the degradation of proton exchange membrane water electrolyzer (PEMWE) with a low catalyst loading of  $0.3 \text{ mg cm}^{-2}$  Pt and  $0.08 \text{ mg cm}^{-2}$  Ir after a long-term test of 4500 hours at  $1.8 \text{ A cm}^{-2}$ . For the first time, the mechanism of cathode degradation is proposed using established physical models from two aspects: (1) Pt dissolution from nanoparticles and (2) Pt dissolution due to rapid Pt oxide reduction at the start of operation. As Ir dissolves and migrates through the membrane, Pt-Ir precipitates are formed in the membrane. Furthermore, iridium dissolution and subsequent re-deposition on the cathode constitute a major portion (42%) of the anode catalyst loss. The overall picture of degradation mechanisms and the distribution of platinum and iridium across the membrane electrode assembly (MEA) are provided.

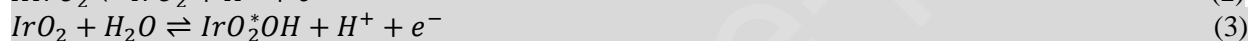
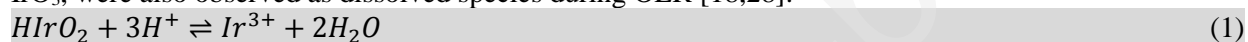
## Keywords:

Proton exchange membrane water electrolysis, membrane electrode assembly, stability, degradation

## 1.0 Introduction

The growing demand for energy calls for a rapid shift from fossil fuels to renewable energy sources, such as wind, solar, biomass, hydropower, and geothermal energy [1]. In the path toward a low-carbon energy society, hydrogen plays an important role as a secondary energy carrier [2-7]. In this context, water electrolysis has the potential to be a key element in coupling the electrical supply, transportation, heating and chemical sectors via power-to-gas in a future sustainable energy system [8,9]. While PEM water electrolysis offers several advantages over traditional electrolysis technologies, further advancement is impeded by insufficient stability of the membrane electrode assembly (MEA) at high anodic potential and high current [10].

The degradation of the MEA in PEMWE has been discussed in several reviews [10-12] as well as studies of high – Pt and Ir – loaded MEAs [13-26] which focus on different components of the MEA. The state-of-the-art anode catalyst for PEM water electrolyzers is iridium oxide. However, iridium suffers from dissolution at high anodic potentials [27] albeit being the most corrosion resistant metal known. The iridium dissolution in a MEA is evidenced by the iridium deposits in the electrolyte membrane [19,21] accompanied by a decrease in both anode exchange current density and overall cell performance [23]. It is proposed that the dissolution of iridium shares the same Ir (III) intermediate species with the oxygen evolution reaction (OER) [18,27-32]. In addition to Ir (III), iridium at higher valences, such as Ir (V) in  $\text{IrO}_2(\text{OH})$  or Ir (VI) in  $\text{IrO}_3$ , were also observed as dissolved species during OER [18,28]:



Being a parallel reaction with OER, iridium dissolution (equation 1 and 6) is inevitable in PEMWE. At low iridium loading, the issues associated with performance degradation are increased [16].

On the other hand, platinum degradation on the cathode has also been reported where platinum nanoparticles were coarsened after long-term operation [22,33]. The contribution of platinum coarsening to the MEA performance loss after long-term operation is limited [22]. However, the stability of the platinum nanoparticles is important in the context of reducing the platinum loading. Paul et al. [26] studied the platinum coarsening and migration on the carbon support and propose that the Pt/C catalysts exhibit a mechanic stress due to  $\text{H}_2$  bubble generation. The formation of a hydrogen monolayer between the platinum particles and carbon support increases with overpotential (or current density), which leads to increased migration rate [26].

In addition to catalyst degradation, the titanium porous transport layer (Ti-PTL) is another main source of MEA degradation [13,22-25]. After long-term operation, a poorly conductive oxide is formed at the interface between Ti-PTL and the electrode, which increases the contact ohmic resistance between the anode and the Ti-PTL [13,22-25]. Titanium dissolution was also observed to affect the activity of the anode catalyst [13,22-25] where the exchange current density of OER was decreased due to titanium contamination. Using a Pt-coated Ti-PTL, the interface is more resistant to oxidation and the Ti dissolution is limited [22]. Thus, the rate of MEA degradation is successfully reduced.

The performance deterioration of PEMWE can also be caused by membrane degradation. The membrane is susceptible to contamination with cations (Ca, Ti, Fe, and Cu) [14] which increases the proton transport resistance. Moreover, the membrane can be attacked by peroxide species generated during OER resulting

in membrane thinning and loss of mechanical integrity [20]. Membrane thinning not only reduces the mechanical strength of the MEA, but also increases hydrogen permeation from cathode to anode, causing a safety issue in the anode oxygen stream where the hydrogen concentration is approaching the lower flammability limit (LFL). Recombination catalysts have been developed to reduce the hydrogen concentration in the oxygen stream by integrating a layer of Pt or Pt-alloy catalyst between the anode catalyst and the membrane [34].

To briefly summarize, different main contributors are defined in various studies and the degradation mechanism of PEMWE MEAs is yet to be fully established. Moreover, only a few studies reported long-term MEA testing at high current density ( $2 \text{ A cm}^{-2}$  or higher) [25,35,36] and studies on low-catalyst-loading MEA are very limited in the field [16]. The cost of high catalyst loading is one of the major barriers for the commercialization of PEMWE technology [37]. Most publications report catalyst loadings on the order of  $1\text{-}3 \text{ mg cm}^{-2}$  for both cathode and anode. The degradation of low-catalyst loading MEAs merits in-depth investigations on catalyst dissolution, re-distribution, and the change of catalyst structure.

In this study, electron microscopy coupled with chemical analysis is utilized to study a low-catalyst-loading MEA after an electrolysis operation of 4500 hours [38]. The MEA was fabricated by a flame-based reactive spray deposition technology (RSDT). The anode catalyst is composed of IrOx nanoparticles embedded in Nafion® ionomer with an iridium loading of  $0.08 \text{ mg cm}^{-2}$ ; while the cathode is platinum supported on carbon black with a platinum loading of  $0.3 \text{ mg cm}^{-2}$ . These loadings are about 3-10% of the loadings that are currently used in state-of-the-art electrolyzers [37]. Cross sections of post-test MEAs are analyzed with scanning electron microscopy (SEM), scanning transmission electron microscopy (STEM), and X-ray energy dispersive spectroscopy (XEDS) to obtain the distribution of catalyst in the MEA and investigate the degradation mechanisms.

## 2.0 Experimental

### 2.1 MEA description and testing

Details of catalyst coated membrane (CCM) fabrication and morphological characterizations can be found in previous work [38]. Briefly, the CCM was prepared using RSDT where anode and cathode catalyst layers were directly deposited onto a piece of Nafion® (N117) membrane. The active area of the CCM was  $86 \text{ cm}^2$ . The anode catalyst was comprised of iridium oxide (IrOx) nanoparticles with an average particle size of 2 nm. The IrOx nanoparticles were embedded in Nafion® ionomer, forming a layer of  $2\text{-}2.5 \text{ }\mu\text{m}$  thickness [38]. The cathode catalyst layer was comprised of platinum nanoparticles supported on Vulcan® XC-72R carbon black with a thickness of  $15\text{-}20 \text{ }\mu\text{m}$ . The average size of platinum particles was 2 nm and the electrode contained Nafion® ionomer for proton conductivity. The Nafion-to-carbon weight ratio of the cathode was kept low at 0.15 to maximize the porosity of the electrode while maintaining sufficient adhesion on the membrane. The anode catalyst layer had an iridium loading of  $0.08 \text{ mg cm}^{-2}$  and the cathode catalyst layer had a platinum loading of  $0.3 \text{ mg cm}^{-2}$  [38]. The MEA was assembled and tested at Nel Hydrogen. Nel's commercially available PEM electrolyzer stack ( $86 \text{ cm}^2$ ) hardware was used for MEA testing. The stability test was conducted at  $80 \text{ }^\circ\text{C}$  at a constant current density of  $1.8 \text{ A cm}^{-2}$  and hydrogen pressure of 2.76 MPa (400 psi) while monitoring the cell potential over a period of 4500 hours (Figure 1) [38].

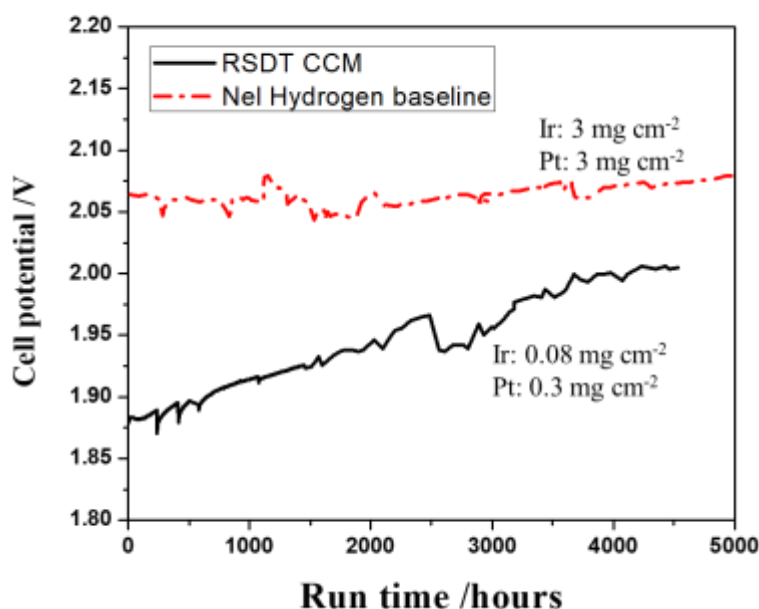


Figure 1. Long-term electrolysis operation of CCM (86 cm<sup>2</sup>) fully fabricated by RSDT process and baseline MEA (86 cm<sup>2</sup>) from Nel Hydrogen [38].

The cell potential of a water electrolyzer MEA reflects the efficiency of converting electrical energy to hydrogen where an increase of cell potential at a fixed current density suggests a decrease of efficiency. Catalyst activity and loading, operating current density, and membrane (which determines ohmic and ionic resistance) are among the most important factors that determine the cell potential. Figure 1 compares the stability performance of RSDT-fabricated CCM with baseline MEA from Nel Hydrogen. The cell potential for the RSDT CCM is lower than that of baseline MEA suggesting that the RSDT-fabricated catalysts have higher voltage efficiency than the baseline MEA. This is likely due to higher catalyst activity (low overpotential for OER) as was demonstrated in [38].

The cell potential for the RSDT CCM at the beginning-of-test is 1.875V (at 1.8 A cm<sup>-2</sup>), which is higher compared to the higher loaded cells in the literature reporting long-term water electrolysis tests using advanced anode catalysts or membranes. The cell potential for those tests using mixed iridium and ruthenium oxides anode catalysts (with high loading ranging from 0.34 to 2 mg cm<sup>-2</sup>) show a cell potential of 1.65-1.75 V at 2 A cm<sup>-2</sup> (at 80 °C) [16,33]. In addition, thinner membranes (90 μm) [39] can further reduce cell potential to about 1.6 V at 2 A cm<sup>-2</sup> (at 80 °C) due to enhanced proton conductivity. Considering the fact that the RSDT-fabricated CCM used Nafion<sup>®</sup> 117 membrane with a thickness of 178 μm and a very low iridium oxide loading of 0.08 mg cm<sup>-2</sup> which has not been reported in the literature, the cell potential is superior to performances reported in the literature

The baseline MEA showed a low degradation rate of cell potential, from almost zero degradation for the first 2000 hours followed by a degradation rate of 11 μV h<sup>-1</sup> for the period of 2000-6000 hours. With the same operating condition as the baseline MEA, the degradation rates for the RSDT MEA was 36.5 μV h<sup>-1</sup> for the initial 2500-hour test period and decreased to 11.5 μV h<sup>-1</sup> for the period of 3500-4500 hours. The literature reported a variety of degradation rates with different operating current density and anode catalyst loading, as summarized in our previous work [38] (Table 7 therein). The degradation rate (μV h<sup>-1</sup>) is a complex measure where all MEA components contribute, the most influential components including membrane, anode electrode, cathode electrode, and titanium porous transport layer (Ti-PTL). In addition,

operating conditions such as operation time, current density, cell potential, and differential pressure affect the degradation rate.

Siracusano et al. [33] explored the relationship of degradation rate ( $\mu\text{V h}^{-1}$ ) with turnover frequency ( $\text{A mg}_{\text{cat}}^{-1}$ ) and thermal power production ( $\text{W mg}_{\text{cat}}^{-1}$ ). In this study, chemical-stabilized Aquivion® membrane (90  $\mu\text{m}$ ) was used and nano-sized IrRu oxide catalyst was used in the anode. Comparing with the relationship presented in [33] (Figure 12 therein), the baseline MEA shows a turnover frequency of 0.6  $\text{A mg}_{\text{cat}}^{-1}$  and thermal power production of 1.23-1.25  $\text{W mg}_{\text{cat}}^{-1}$ . The degradation rate is negligible for the initial 2000 hours and increased to comparable values as predicted in [33] (Figure 12 therein) for the period of 2000-6000 hours. The RSDT CCM shows a turnover frequency of 22.5  $\text{A mg}_{\text{cat}}^{-1}$  and thermal power production of 42-45  $\text{W mg}_{\text{cat}}^{-1}$ . Although both values are beyond the range of Figure 12 in [33], the measured degradation rate is lower than predicted in [33], confirming the superior performance of RSDT MEA.

It should be noted that the trend predicted in [33] is based on a different anode catalyst than RSDT MEA and was operated for 1000 hours compared to ~4500 hours for the RSDT MEA. Additionally, the active area used in [33] was 5  $\text{cm}^2$ , much smaller compared to our previous work [38], 86  $\text{cm}^2$ . The size of the active area could affect the distribution of current, potential, and mass transport during electrolysis operation. Therefore, the active area is another factor to be considered when evaluating degradation rates in future studies.

## 2.2 Microscopic analysis

Morphological and physical-chemical characterizations were carried out on the post-test CCM. Small strips of CCM were cut from the edge and center of the CCM (Figure S1). The edge is considered a non-degraded CCM location since it was under the sealing surface. The center of the CCM is representative of the degraded CCM. The strips were embedded in epoxy and slices of the epoxy sample mount (~100 nm thick) were then cut using a LEICA ultramicrotome and deposited on a copper grid for transmission electron microscopy (TEM) observation.

TEM observations were performed on Talos TEM (Thermo Fisher Scientific) with a field-emission source at 200 keV. High-angle annular dark field (HAADF) images were obtained for morphology, particle size, and chemical composition analysis. X-ray energy dispersive spectroscopy (XEDS) mapping was obtained using Super-X system (containing 4 silicon drift detectors). The quantitative analysis of XEDS data was processed with Esprit 1.9 software (Bruker). The atomic composition of platinum and iridium was analyzed with L lines in the spectrum using Cliff-Lorimer k factors given by the Esprit 1.9 software.

Scanning electron microscopy (SEM) characterization and XEDS analysis of the cross section was performed on epoxy blocks in which the strip of CCM was embedded. The surface morphology and electrode thickness were characterized by Quanta SEM (Thermo Fisher Scientific) with a field-emission source and Everhart-Thornley (secondary electron) detector. The quantitative XEDS analysis was performed on Apex software.

## 3.0 Results and discussion



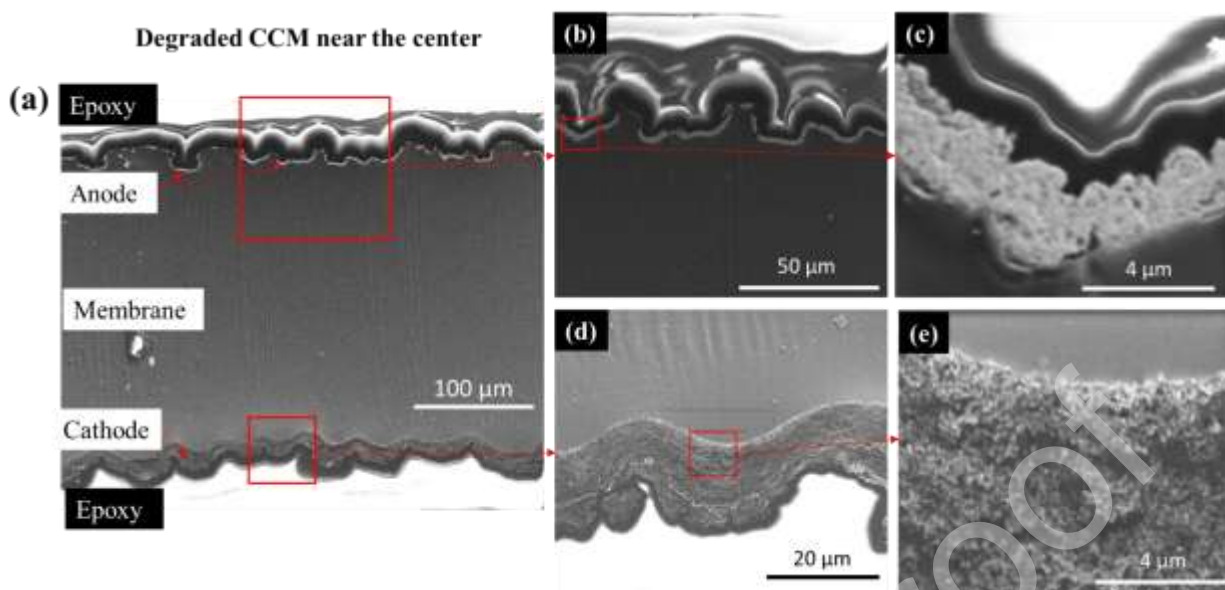


Figure 2. Cross-sectional SEM images of degraded CCM near the center where (a) shows the entire cross section; (b, c) show the magnified anode region; and (d, e) show the magnified cathode region.

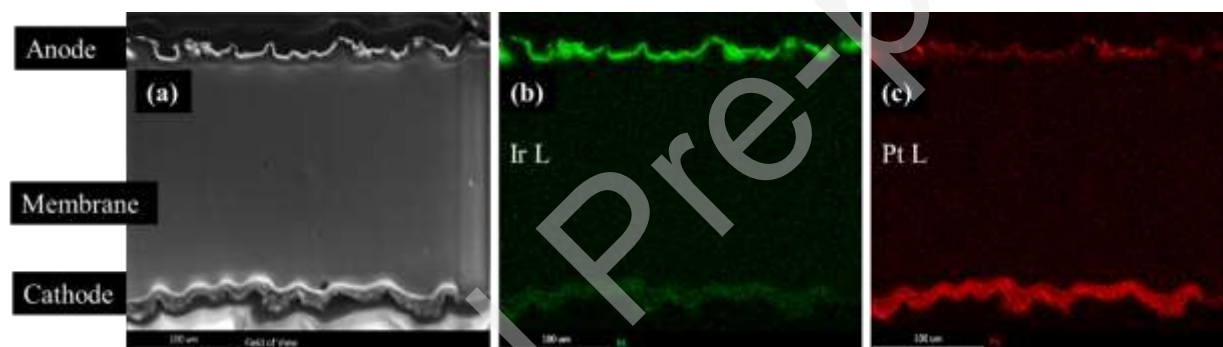


Figure 3. XEDS mapping of Ir and Pt distribution across the CCM using SEM. (a) is the mapped region where the entire CCM cross section is displayed. (b) and (c) shows the map of Ir and Pt, respectively.

The cross section of the degraded CCM is shown in Figure 2 where both anode and cathode catalyst layers are wrinkled due to compression during cell assembly and drying out upon disassembly. The anode shows a thickness of 2-2.5  $\mu\text{m}$ , while the cathode thickness is measured between 14-22  $\mu\text{m}$ . XEDS maps of the cross section are displayed in Figure 3 where strong Ir and Pt signals are observed at anode and cathode catalyst layers, respectively, as expected. It is noted that weak signals of Ir can be seen in the cathode and the membrane region (Figure 4b), and weak signals of Pt can be seen in the anode and the membrane region (Figure 3c). Particularly, the Pt signals on the anode are inhomogeneous where a few spots show higher intensity than the rest of the anode. Such strong Pt signals on the anode can be attributed to the residual Pt from the Pt-plated Ti porous transport layer (PTL). The possibility of the weak Ir signal as a result of X-ray fluorescence can be ruled out with high-resolution STEM-XEDS maps and electron energy-loss spectroscopy (EELS) in the following discussions. It is noted that EELS results were not used for quantification because the Pt and Ir peaks have low intensity compared to the plasmonic peak from carbon and oxygen.

Further verification of Ir and Pt distribution is shown in Figure S2 and S3. Figure S2 compares the spectrum of two regions from the anode with (Figure S2b) or without (Figure S2c) the residual Pt from the Ti-PTL. Without the residual Pt, no Pt  $L\alpha$  peak is observed in the spectrum (Figure S2c) of the anode region, which

confirms that the presence of Pt (Figures 2c and Figure S2b) is due to the residual Pt from the Pt-plated Ti PTL. Note that the Cl signal in Figure S1b and S1c comes from the epoxy in which the specimen is embedded. The spectrum in membrane and cathode regions are displayed in Figure S3. The membrane regions (Figures S3b and S3c) does not show any Pt L $\alpha$  peak or Ir L $\alpha$  peak, suggesting that the Pt and Ir signals in the membrane (Figures 3b and c) are due to the background signal. However, this does not preclude the possibility of the existence of Pt or Ir precipitates in the membrane because the particles could be too small to provide sufficient signals in SEM. The spectrum from the cathode region (Figure S3d) shows both Pt L $\alpha$  peak or Ir L $\alpha$  peak, indicating that both Pt and Ir are present in the cathode at end-of-test (EOT). We hypothesize that Ir is dissolved during MEA testing and migrates towards the cathode where it is re-deposited. However, further evidence is needed and detailed examination with TEM are presented in the following discussions.

Specimens for TEM cross-sectional analysis were prepared using ultramicrotome. Figure S4 shows a low-magnification image of the section displaying both anode and cathode catalyst layer. The membrane exhibits low mechanical integrity due to the degradation from long-term MEA testing and thus was partially ripped during ultramicrotome preparation. For the following discussions, images of the cathode catalyst layer are oriented such that the membrane is at the bottom of the image (Figure S4b), which is consistent with images of the anode. Two regions were selected from the post-test CCM (Figure S1) for ultramicrotome, one at the edge (under the sealing surface) representing the non-degraded CCM and one at the center (active area) representing the degraded CCM.

### 3.1 Anode degradation

Figures 4a and c compare the non-degraded and degraded anode catalyst layer by STEM-XEDS. The differences in the contrast within the anode catalyst layer can be attributed to variations in the IrO $_x$ /Nafion<sup>®</sup> agglomerates. The catalyst deposition process produces IrO $_x$ /Nafion<sup>®</sup> agglomerates in a variety of sizes and porosity, and this can be reflected as varied mass-thickness contrast when thin specimens are sliced from the bulk sample. It is also noted that the non-degraded anode is thinner than the degraded anode. It is likely that the edge under sealing surface experiences higher compression, evidenced by the visual observation (Figure S1) of the imprint at the edge.



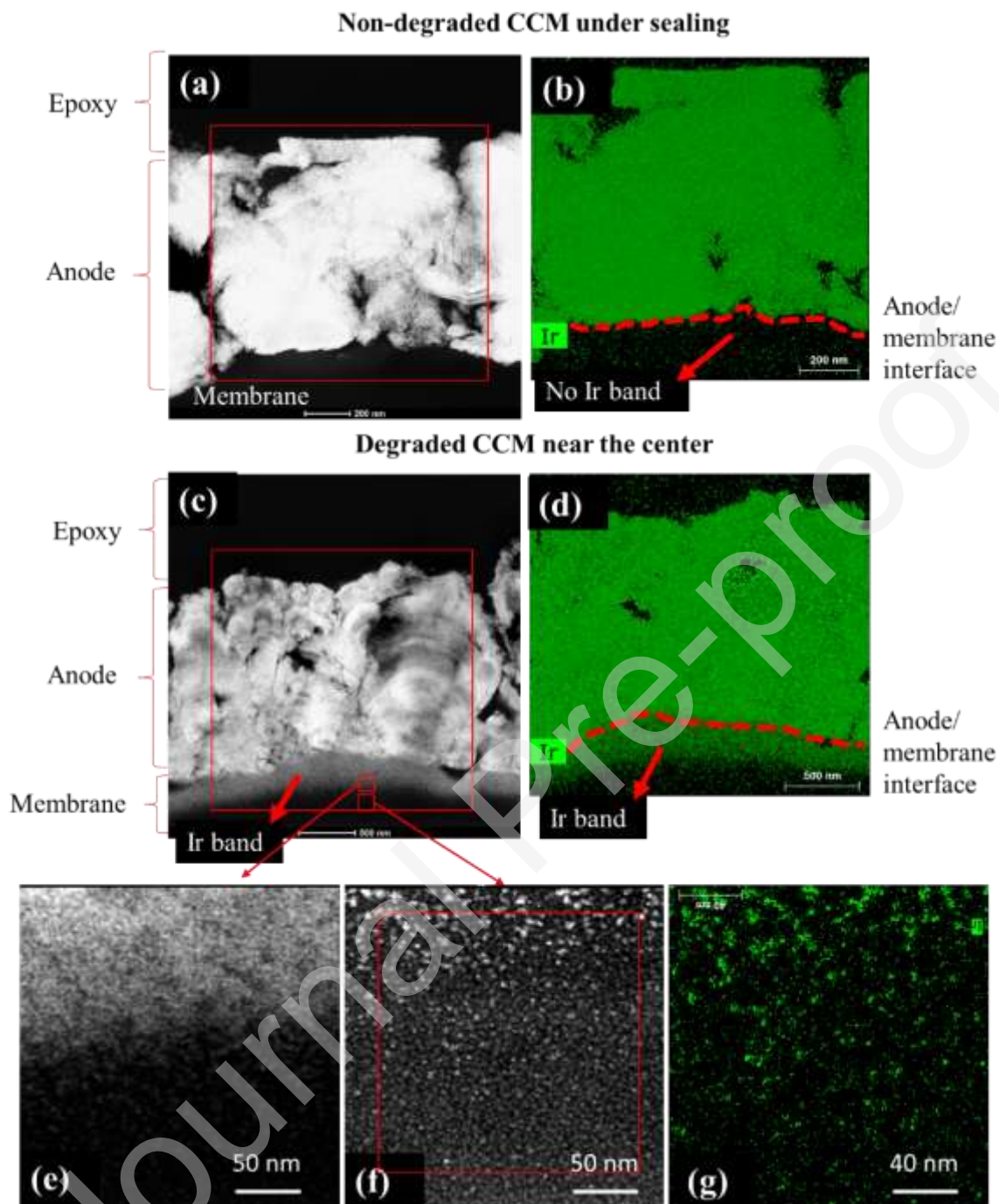


Figure 4. (a-d) Comparison of non-degraded and degraded anode catalyst layer and the anode/membrane interface. (b) and (d) show the elemental mapping of Ir for (a) and (c), respectively. (e, f) are high-magnification images of the Ir band and its boundary in the membrane. (g) shows the elemental mapping of Ir for (f).

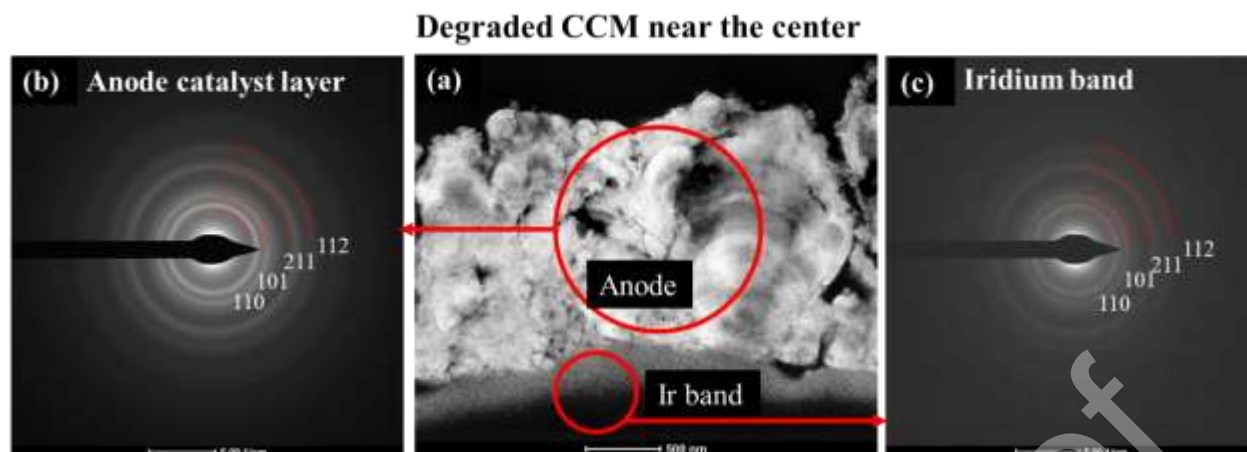


Figure 5. (a) STEM image of degraded anode. (b) and (c) Selected-area electron diffraction (SAED) pattern of degraded anode catalyst layer and the Ir band, respectively.

The degraded specimen shows a strong Ir band extending  $\sim 500$  nm from the anode/membrane interface into the membrane (Figures 4a-d). This is direct evidence of iridium dissolution during the electrolysis operation at  $1.8 \text{ A cm}^{-2}$  where the anode potential is measured 1.9-2.0 V. The accumulated counts of Ir signal in the regions of anode and Ir band have a ratio of 3:1, which can be approximated to the Ir mass ratio since the thickness of the ultramicrotome section is homogeneous and approximately 100 nm. High-magnification images of the band reveals that the Ir band is composed of small particles (Figures 4e, 4f). The density of the particles in the Ir band decreases gradually toward the membrane (Figures 4f, 4g). Further examination of the degraded CCM with selected-area electron diffraction (SAED) (Figure 5) shows that the material of the anode catalyst layer (Figure 5b) and the Ir band (Figure 5c) are both iridium oxide with the diffraction rings exhibiting a tetragonal structure. The calculated d-spacings are verified with JCPDS (00-043-1019) (Tables S1 and S2). Furthermore, the XEDS mapping (Figure 4) shows no Pt in the anode after operation based on the spectrum (Figure S5), which agrees with the results from SEM (Figure S2c).

### 3.2 Cathode degradation

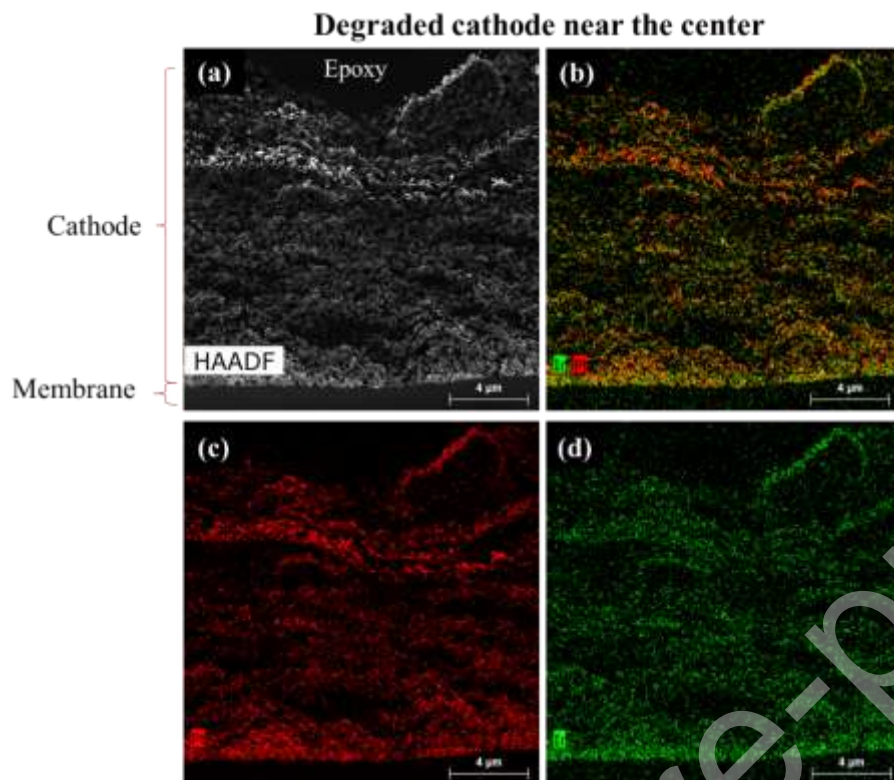


Figure 6. (a) Degraded cathode catalyst layer and (b-d) XEDS mapping of Pt and Ir.

The degradation of the cathode is dominated by Ir deposition and Pt migration. Figure 6 shows the entire cross section of the degraded cathode. The co-existence of Pt and Ir in the degraded cathode is evidenced from XEDS maps (Figures 6b-d), in agreement with the observation in SEM (Figure 3c and Figure S3d). It is noted that the cathode/membrane interface shows a strong intensity of Pt and Ir. Quantification of XEDS analysis shows that the atomic ratio of Pt/Ir is 7.7 across the cathode (Figure 6). Further examination (Figure 7a) reveals that the concentration of Pt and Ir both increase toward the cathode/membrane interface, and that the concentration profile exhibits a sharp increase within 1 μm from the interface. The gradual decrease of Ir concentration away from the interface indicates that the Ir migration follows the direction from anode to cathode. This supports the observation of Ir dissolution and re-deposition, which results in the formation of the Ir band at the anode and Ir deposition on the cathode. The gradual change of the Pt concentration profile suggests that Pt dissolves and migrates during MEA testing following the direction from cathode to anode. This has not been reported in any previous literature. The direction of Pt ion migration is similar to that of a PEM fuel cell cathode where the Pt loss is so significant that it leads to Pt depletion [39,40]. Thus, for a fuel cell cathode, the Pt concentration decreases towards the membrane. In case of an electrolyzer cathode, the Pt loss is less significant than that in a fuel cell. Thus, we observe an accumulation of Pt at the cathode/membrane interface due to Pt re-deposition, instead of a Pt depletion zone, and the profile of the electrode exhibits higher Pt concentration towards the membrane. Further verification of Pt dissolution in the cathode will be discussed in section 3.4.

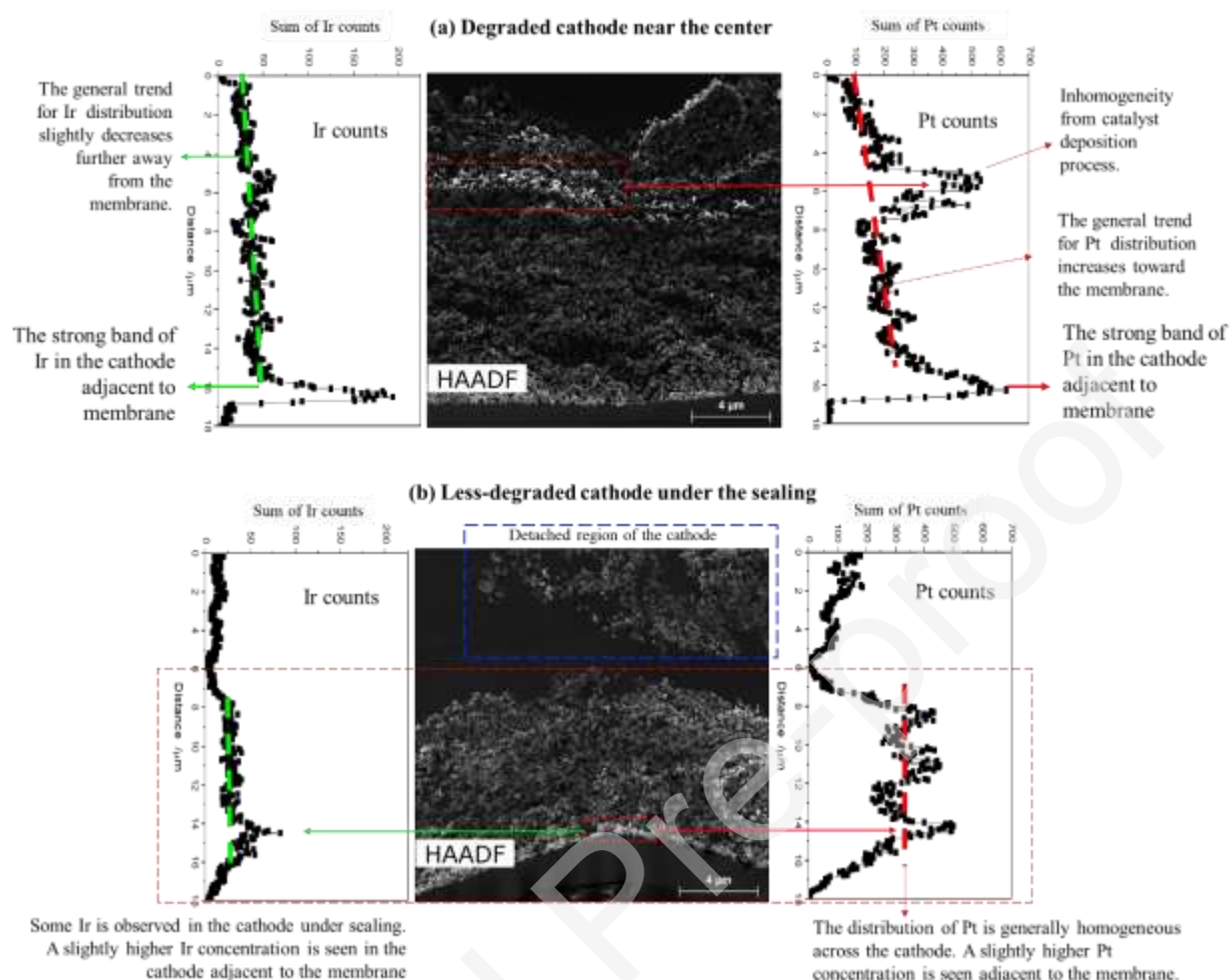


Figure 7. (a) Profiles of Ir and Pt counts summarized across the degraded cathode near the center. (b) Profiles of Ir and Pt counts summarized across the less-degraded cathode under the sealing.

The overlay of Pt and Ir maps in Figure 6b shows that the Pt and Ir signals are significantly overlapped, indicating that Ir is deposited on Pt. To further reveal the structure of Ir deposition, high-resolution imaging and XEDS mapping were obtained at different locations of the degraded cathode. It can be confirmed from these high-resolution maps (Figures 8, 9, S6-S11) that the Ir signal is not a result of X-ray fluorescence. Figure 8 shows an example of a high-resolution map of a 203 nm by 203 nm region of the cathode catalyst adjacent to the membrane. The particles are coarsened and form a dendritic shape where multiple particles are connected. The coarsening of Pt at the cathode was also observed in [22]. It is likely that the Pt migration, as indicated in Figure 7, increased the concentration of Pt ions adjacent to the membrane and then re-deposited on existing Pt particles. Figure 8 shows the cathode region adjacent to the membrane. The elemental distribution of Pt (Figure 8b) agrees with the HAADF image of Pt-Ir particles in Figure 8a. The distribution of Ir, however, is different than the distribution of Pt, and the overlay of Pt and Ir maps shows that Ir is distributed on the edges of the Pt particles. Further examination of multiple spots in the map (Figure 9) reveals that the Pt/Ir atomic ratio is higher when the spot is located at the center of a particle, indicating that the particle has a Pt-rich center. At the edge of the particle, the Pt/Ir ratios are always lower than that at the center, indicating an Ir-rich edge. Thus, it is evident from high-resolution XEDS mapping that Ir is deposited on the surface of Pt particles. Figures S7-S12 further support this observation at different locations of the cathode with various particle sizes. In particular, Figures S6 and S7 show another region of cathode catalyst adjacent to the membrane where the particle size is smaller than that in Figures 8 and 9.



The Pt/Ir ratio at the center of the particles (Figure S7) has lower values than that in Figure 9, in agreement with the smaller particle size. Figures S8 and S9 show a cathode region mid-way from the membrane, and Figures S10 and S11 show a cathode region at the top of the cathode (farthest from the membrane). It should be noted that the oxygen maps in Figures 8, S6, S8, and S10 exhibit a pattern where the locations of Pt-Ir particles have weak intensity of oxygen. This suggests that the Pt-Ir particles in the cathode do not contain oxygen, that is, the particles remain metallic after operation. In summary, Ir is deposited on the surface of Pt particles throughout the entire cathode, and there is no evidence of an alloy structure for the Pt-Ir particles.

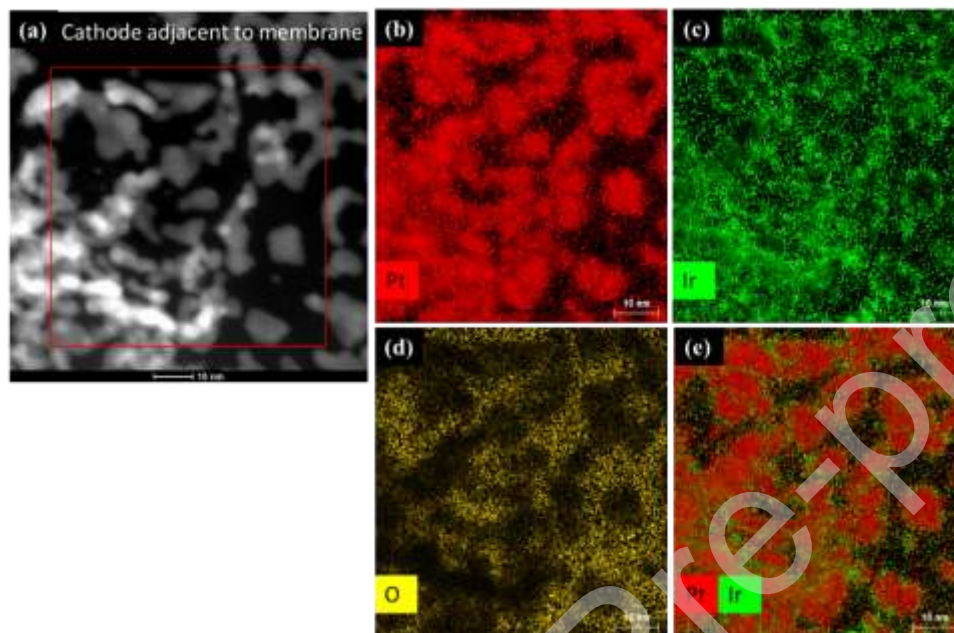
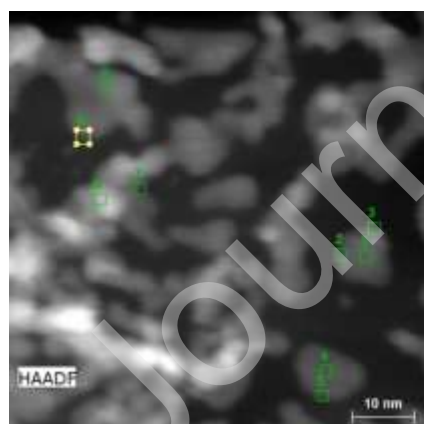


Figure 8. High-magnification EDX mapping of cathode catalyst adjacent to membrane: (a) shows the region being mapped (red box); (b) Pt map; (c) Ir map; (d) O map; and (e) overlay of Pt and Ir maps. The atomic ratio of Pt to Ir is 4.0.



Spot	Pt/Ir ratio
1	22.70811
2	3.406874
3	2.086093
4	9.539295
5	1.316276
6	8.900362
7	3.067296
8	21.15525
9	2.271795

Figure 9. Examination of Pt/Ir atomic ratio at centers and edges of various particles for Figure 8.

The “non-degraded cathode” under sealing was also examined with STEM and XEDS (Figures 7b and 10). Surprisingly, iridium was found in the cathode region (Figure 10b and c) and Pt/Ir precipitates were present in the membrane (Figures 10e and f). Thus, instead of “non-degraded cathode,” “less-degraded cathode” is more appropriate for the description. The Pt/Ir atomic ratio is 4.5 for the cathode catalyst adjacent to the membrane (Figure 10b), which is comparable with the degraded cathode (Figures 8, S6, S8, and S10). The Pt/Ir atomic ratio increased to 49 about half-way into the cathode (Figure 9c), corresponding to only 2% Ir

and no Ir was detected at the top of the cathode (Figure 10d). The Ir deposition under the sealing area is only pronounced at the cathode/membrane interface. This is in agreement with the anode under sealing (Figures 4a and b) where less iridium dissolution is seen compared to the degraded anode. Since iridium cations migrate from the membrane toward the cathode, less iridium concentration will most likely be deposited at the cathode/membrane interface and therefore have less chance of moving further into the cathode. It is noted that the concentration profile of Pt of the “less-degraded cathode” (Figure 7b) is in general homogeneous except for a few local variances. This indicates that the Pt dissolution is not as pronounced compared to the “degraded cathode” (Figure 7a).

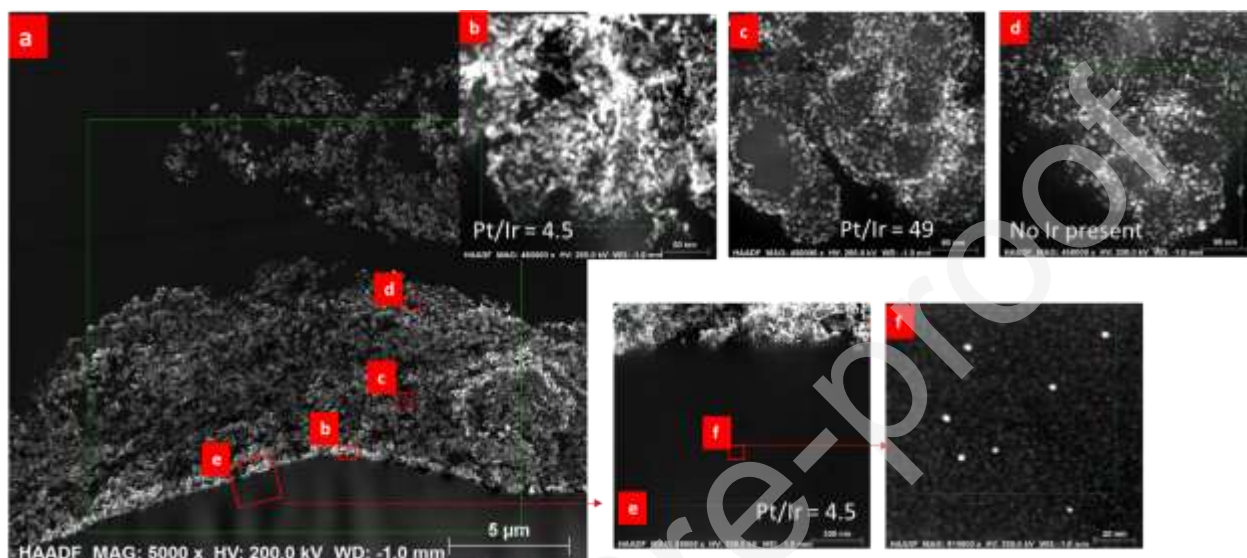


Figure 10. (a) Less-degraded cathode catalyst layer (under sealing) and (b-f) enlarged area of XEDS mapping and corresponding Pt/Ir atomic ratio.

### 3.3 Membrane degradation

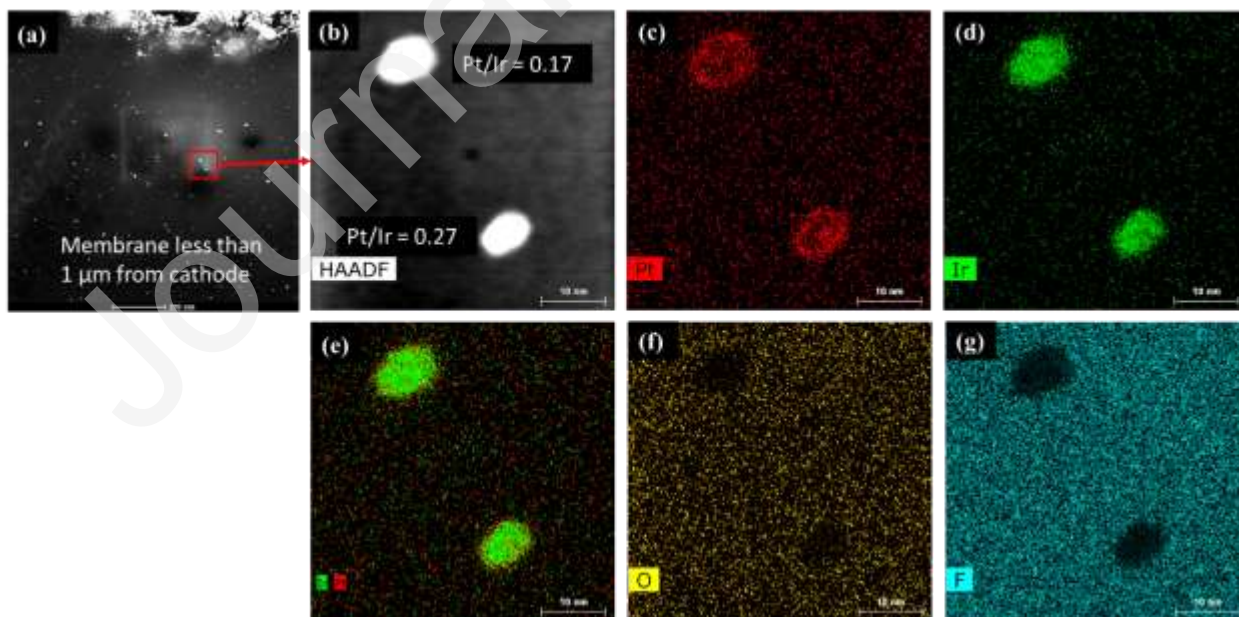




Figure 11. (a) HAADF image of Pt-Ir particles in the membrane near the cathode. (b) High-magnification HAADF image of the Pt-Ir particles in the membrane. (c) and (d) show the XEDS maps of Pt and Ir, respectively. (e) shows the overlay of Pt and Ir maps. (f) and (g) show the XEDS maps of O and F.

In addition to the loss of mechanical integrity due to chemical degradation (Figure S4), the membrane suffers from deposition of ionic Pt and Ir species. As hydrogen diffuses from the cathode to the anode through the membrane, ionic Pt and Ir species are reduced to metallic particles similar to what happens in a PEMFC [39,40]. Figure 11a shows the membrane region within 1  $\mu\text{m}$  from the cathode/membrane interface. A large number of particles (bright dots) can be observed in the membrane. High-magnification images show that these particles range from 5 nm to 10 nm diameter (Figure 11b, Figure S13). XEDS mapping reveals that the large particles ( $\sim 10$  nm) contain both Pt and Ir (Figure 11c-e). The Pt-to-Ir atomic ratio less than 1 obtained from the spectrum (Figure 11b) indicates that the particles are Ir-rich. The elemental mapping of Pt suggests that the particle has a Pt-rich shell. This is confirmed with further examination of Pt-to-Ir atomic ratio within the particle (Figure S12). Small particles ( $\sim 5$  nm) (Figure S13) show a Pt-to-Ir atomic ratio greater than 1, which indicates that the particles are Pt-rich. An XEDS map was not successful due to the drift of small particles while imaging. To reduce the effect from drift, line scans were used to obtain XEDS spectrum with shorter collection time. The profile of Pt and Ir signals across the particles (Figure S13e) are in agreement, suggesting a homogeneous distribution of Pt and Ir within the small particle. The profile in the Y direction was off-centered (Figure S13f) because the particle was drifting in the Y direction when imaging.

Figure S14a shows the Pt-Ir deposits in the membrane at 15  $\mu\text{m}$  from the cathode/membrane interface. The difficulty of imaging Pt-Ir deposits at other locations, i.e. 20  $\mu\text{m}$ , 50  $\mu\text{m}$ , and further away from the cathode/membrane interface was greatly increased due to the chemical degradation of the membrane. Thus, imaging with low electron dose was attempted (Figures S14b-g) where the objective aperture of the TEM was located on the most intense electron diffraction rings from Pt-Ir deposits. Pt-Ir deposits appear as bright dots in HAADF images (Figures S14b-g). While reduced electron dose limits the number of observable Pt-Ir deposits as the objective aperture selects only a fraction of the electron diffraction ring, this allows Pt-Ir deposits to be distinguishable in the membrane  $\sim 90$   $\mu\text{m}$  away from the cathode/membrane interface, approximately half-way across the entire CCM. Almost no particles can be seen beyond 90  $\mu\text{m}$ . The bright dots at the center of Figure S14b-g are caused by beam damage.

It is worth noting that the XEDS maps of Pt-Ir deposits (Figure 11f) show that the particle has very weak signals of oxygen, similar to the Pt-Ir particles in the cathode (Figures 8, S6, S8, and S10). This indicates that the Pt-Ir deposits (less than 1  $\mu\text{m}$  from cathode) are metallic. However, high-magnification maps were unable to obtain due to particle drift at these locations and more work is needed to analyze Pt-Ir deposits further away from the cathode. Further, confirmation of the oxidation state of Pt and Ir with electron energy-loss spectroscopy (EELS) was not successful due to the influence of strong plasmon signal (caused by carbon and ionomer) on the resolution of Pt and Ir peaks in the spectrum. The same issue was encountered with EELS analysis on the anode and cathode catalyst.

### 3.4 Discussion

The degradation of a CCM after long-term water electrolysis operation was thoroughly examined in sections 3.1-3.3. While the mechanism of Ir dissolution and migration is similar to that of Pt in a fuel cell cathode [39,40], the mechanism of Pt dissolution and migration remains elusive. There are two possible sources of Pt dissolution: the Pt-coated Ti PTL on the anode side and the Pt catalyst on the cathode side. The degradation of the Ti PTL has been studied in detail [22-24] where aged MEAs show a significant amount of Ti in the cathode electrode and membrane regions. The contamination of cathode electrode and the membrane with Ti cations reduces both the catalytic activity and the proton conductivity, which result in irreversible damage to the CCM [12,22]. In addition, Pt is found in the anode region of the aged MEAs

which indicates that the Pt coating on the Ti PTL dissolves and some of the produced Pt cations migrate to the anode [22,23].

In the present study, Pt is not detectable in the anode region of the CCM with XEDS mapping in Figure 4. The signal of Ti is very weak, accounts for only 0.17 wt.% in the anode region, and is much lower than the Ir content (59.7 wt.%). The cathode region (Figure 6) shows a Ti content of 0.26 wt.% and is also much lower than the Pt content (44.3 wt.%). Furthermore, Ti is not detectable in the membrane region either near the cathode (Figure 10) or near the anode (Figure 4f). Non-detectable Pt content in the anode and the low content of Ti across the CCM suggest that the degradation of the PTL is very limited. Thus, the contribution of Pt dissolution from the Pt coating on the PTL is not identifiable to account for the observed Pt precipitates in the membrane.

To better understand the Pt dissolution process at the cathode of PEMWE, we first estimate the amount of Pt and Ir in the membrane precipitates. The particle size in Figure 11a and Figure S14a were analyzed with ImageJ software. Since the particle contains both Pt and Ir, the specific density of the particle is:

$$\rho_{Pt-Ir} = X_{Pt} \cdot \rho_{Pt} + X_{Ir} \cdot \rho_{Ir} \quad (8)$$

where  $X_{Pt}$  is the mass fraction of Pt;  $\rho_{Pt}$  the density of Pt (21.45 g/cm<sup>3</sup>);  $X_{Ir}$  is the mass fraction of Ir;  $\rho_{Ir}$  the density of Ir (22.56 g/cm<sup>3</sup>).  $X_{Pt}$  and  $X_{Ir}$  are determined from XEDS quantification. The XEDS mapping of membrane precipitates in Figure 11a and S14a show that the atomic ratio of Pt to Ir is ~55:45. The total mass of particles (g) in the image is:

$$M_{Total} = \sum_{i=1}^N \frac{4}{3} \pi r_i^3 \cdot \rho_{Pt-Ir} \quad (9)$$

The Pt mass (g) is thus:

$$M_{Pt} = X_{Pt} \cdot M_{Total} \quad (10)$$

The Pt concentration (g cm<sup>-3</sup>) is estimated with the image size (S, cm<sup>2</sup>) and specimen thickness, t (~100 nm, or 10<sup>-5</sup> cm):

$$C_{Pt} = \frac{M_{Pt}}{S \cdot t} \quad (11)$$

The total volume (cm<sup>3</sup>) in the membrane per 1 cm<sup>2</sup> active area is:

$$V = \frac{T_{MEM}}{2} \cdot 1 \quad (12)$$

where  $T_{MEM}$  is the thickness of N117 membrane (178 μm, or 0.0178 cm). Note that the factor of 2 is added because precipitate particles were observed in half of the membrane toward cathode (Figure S14).

Finally, the Pt mass loss% due to precipitation in the membrane is:

$$Pt_{lost\%} = \frac{C_{Pt} \cdot V}{10^{-3} \cdot L_{Pt} \cdot 1 \text{ cm}^2} \cdot 100 \quad (13)$$

where  $L_{Pt}$  is the cathode Pt loading, 0.3 mg cm<sup>-2</sup>. Analysis of Pt-Ir particle size distribution of Figures 11a and S14a results in 4-6×10<sup>-16</sup> g of Pt in the imaged area, which is equivalent to a Pt concentration of 2-4×10<sup>-3</sup> g cm<sup>-3</sup> in the membrane. Thus, the Pt lost % in the membrane is about 7-11%.

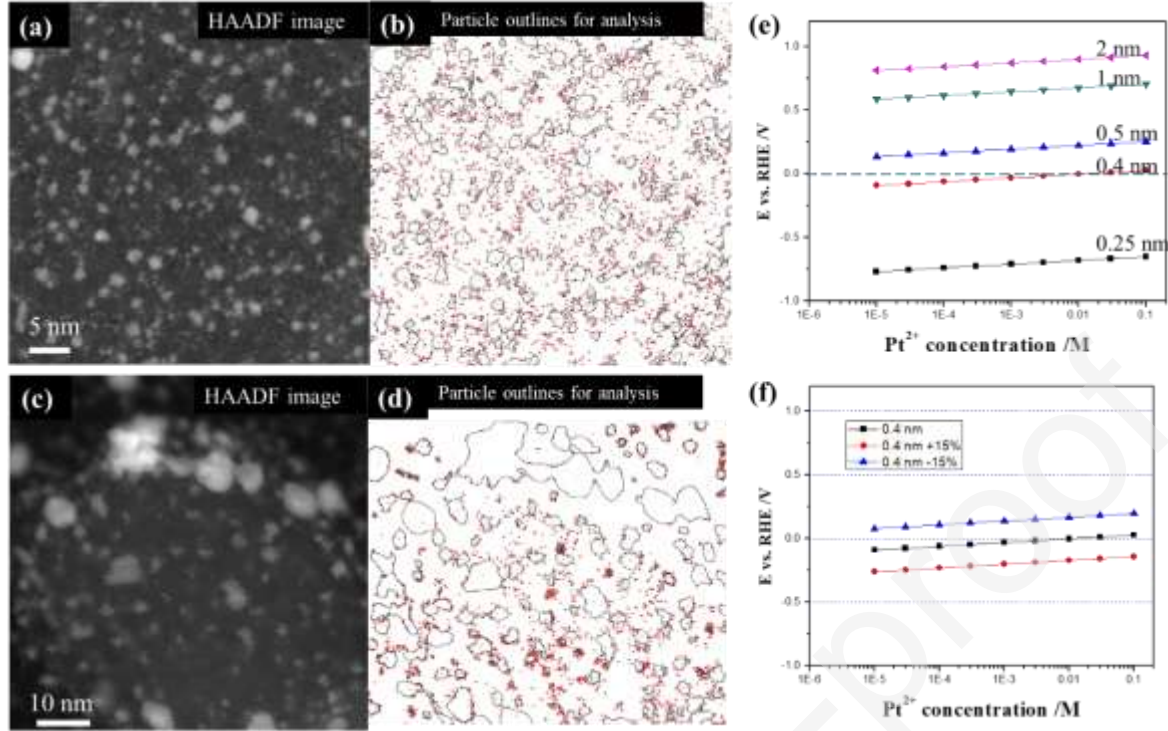


Figure 12. (a) and (b): estimation of Pt particle size and mass distribution on supported and unsupported, respectively, Pt particles from RSDT process. (c) and (d) are the processed particle outlines for size distribution analysis for (a) and (b), respectively. (e) Equilibrium potential calculated from Gibbs-Thompson relation for Pt nanoparticles in a concentration range estimated for the cathode of PEMWE. (f) The range of equilibrium potential calculated with 15% variance of Pt surface energy.

The next step is to estimate the amount of Pt dissolution in the cathode and compare with the estimated Pt found as precipitation in the membrane. Pt dissolution and migration are well known in fuel cell studies [39-42] where Pt dissolves during drive cycles between 0.6V and 1.0-1.4V and Pt ions migrate toward the membrane based on Fick's diffusion law. Due to the Gibbs-Thompson relation, the potential at which a Pt nanoparticle is stable decreases with the decrease of Pt particle size [43-45]. Thus, it is possible that small particles dissolve at a lower potential window than the drive cycles of a fuel cell. To estimate the amount of Pt dissolution, the Pt particle size at beginning-of-test (BOT) with high-resolution (HR) STEM imaging was measured. The Pt particles produced from the flame were either directly collected on the TEM grid or supported on Vulcan XC-72R. Figures 12a-d and S15a-d displays the analysis of Pt particles size at BOT. Many Pt clusters below 1 nm diameter are shown in Figures 12 and S15 in addition to Pt nanoparticles.

The calculation of Pt loss due to direct dissolution is based on the method introduced in [43]. The direct dissolution can be expressed as:



With an equilibrium potential of:

$$\bar{E}_{\text{Pt}/\text{Pt}^{2+}} = \bar{E}_{\text{Pt}/\text{Pt}^{2+}}^0 + \frac{2.303RT}{nF} \log[\bar{\text{Pt}}^{2+}] \quad (15)$$

which is a function of  $\text{Pt}^{2+}$  concentration only. In this equation,  $\bar{E}_{\text{Pt}/\text{Pt}^{2+}}^0 = 1.188 \text{ V}$  is the equilibrium potential at standard temperature, pressure, and  $\text{Pt}^{2+}$  concentration.  $R$  is the gas constant ( $8.314 \text{ J mol}^{-1} \text{ K}^{-1}$ );  $T$  is temperature (K);  $F$  is Faraday's constant ( $96485 \text{ C mol}^{-1}$ );  $n$  is the electron transfer number ( $n=2$ ).

The  $\text{Pt}^{2+}$  concentration in the cathode electrode is calculated with the assumption that Pt particles below a certain size completely dissolve and become  $\text{Pt}^{2+}$ . Taking, for example, a threshold of 0.4 nm, the mass fraction of all Pt particles  $< 0.4$  nm diameter is:

$$f_{\text{Pt}<0.4 \text{ nm}} = \frac{\sum_{i=1}^N \frac{4}{3}\pi r_i^3 \cdot \rho_{\text{Pt}} (r_i \leq 0.2 \text{ nm})}{\sum_{i=1}^K \frac{4}{3}\pi r_i^3 \cdot \rho_{\text{Pt}} (r_i \geq 0.2 \text{ nm})} \quad (16)$$

The  $\text{Pt}^{2+}$  concentration (mol/L) is:

$$C_{\text{Pt}} = \frac{f_{\text{Pt}<0.4 \text{ nm}} \cdot L_{\text{Pt}} \cdot 10^{-3} / M}{S \cdot t \cdot 10^{-7}} \quad (17)$$

Where  $L_{\text{Pt}}$  is the cathode Pt loading,  $0.3 \text{ mg cm}^{-2}$ ;  $M$  is the molar weight of Pt ( $195.084 \text{ g mol}^{-1}$ );  $S$  is an area of  $1 \text{ cm}^2$ ;  $t$  is the electrode thickness ( $15 \text{ }\mu\text{m}$ ). The size-dependent equilibrium dissolution potential,  $E_{\text{Pt}/\text{Pt}^{2+}}(r)$ , is derived based on Gibbs-Thompson relation [43]:

$$E_{\text{Pt}/\text{Pt}^{2+}}(r) = \bar{E}_{\text{Pt}/\text{Pt}^{2+}} - \frac{\gamma_{\text{Pt}} \Omega_{\text{Pt}}}{nF \cdot 10^{-9}} \left( \frac{2}{r} \right) \quad (18)$$

where  $r$  is the particle radius (nm);  $\gamma_{\text{Pt}}$  is the surface energy of Pt from first-principles calculation ( $2.4 \text{ J m}^{-2}$ );  $\Omega_{\text{Pt}}$  is the volume of a unit cell for Pt FCC crystalline ( $9.09 \times 10^{-6} \text{ m}^3$ ). Thus, with a Pt particle size threshold of 0.4 nm diameter, the  $\text{Pt}^{2+}$  concentration for Figure 12a is  $10^{-2} \text{ M}$  corresponding to an equilibrium potential of 0.0V (-0.17V to +0.17V). The  $\text{Pt}^{2+}$  concentration for Figure 12c is  $10^{-3} \text{ M}$  corresponding to an equilibrium potential of -0.031V (-0.206V to +0.134V).

Using the method in [43], the potential of Pt particles/clusters in equilibrium with  $\text{Pt}^{2+}$  is calculated in Figures 12e and f with a  $\text{Pt}^{2+}$  concentration in the range of  $10^{-5}$  to  $10^{-1} \text{ M}$ . As the Pt particle size decreases from 2 nm to 0.25 nm, the equilibrium potential decreased from  $\sim 0.8\text{V}$  to  $\sim -0.6\text{V}$  (vs. RHE). At about 0.4 nm, the equilibrium potential is around 0V and thus particles below 0.4 nm are likely to be dissolved during water electrolysis. This agrees with high-magnification HAADF images (Figures 8, S7-S12) where no Pt clusters are present after long-term operation. Based on Figures 12 and S15, the dissolved Pt particles account for  $\sim 1\%$  mass of the cathode Pt loading, which is less than an estimated 7-11% loss of Pt to the precipitates in the membrane. It is noted in [43] that the possible variance in the equilibrium potential calculation stems from the estimation of surface energy parameters. Figure 12f shows the possible range of equilibrium potential of 0.4 nm Pt particles with a 15% variance on the surface energy of Pt suggested in [43]. However, even at the lower range of equilibrium potential, i.e. more Pt particles are dissolved, the source of the remaining 6-9% of Pt loss remains to be identified.

We hypothesize that the source of the remaining Pt in the membrane stems from the Pt that is dissolved during the transient period at the start of the MEA test. Significant Pt dissolution is reported during the Pt surface oxide reduction where the potential sweeps rapidly from 1.0-1.2V to 0.6V or lower potentials [42]. An oxide layer is formed on the Pt surface during MEA fabrication. Since the cathode is saturated with air, the cathode potential is  $\sim 1.0 \text{ V}$  at the start of the MEA test. As the test progresses, the cathode potential decreases rapidly with the increase of current (and hydrogen production) from above 1.0V to below 0V. Pt oxide is reduced and dissolved at and below 0.6V during this transient change of cathode potential. Thus, the Pt oxide at the BOT will also contribute to the total Pt lost from the cathode. To verify this hypothesis, the amount of Pt oxide at BOT is estimated based on XPS results and the theoretical number of surface Pt atoms for a particle. The amount of surface Pt oxide is 30% from XPS analysis in our previous work [46]. To obtain the mass fraction of surface Pt, we employed the relation of surface atomic number vs particle size calculated by Wang et al., 2005 [47]. Based on the particle size analysis of Figure 11 and S15, the mass of Pt surface atoms can be calculated as:

$$M_{\text{Pt,surface}} = \sum_{i=1}^N \frac{4}{3}\pi r_i^3 \cdot \rho_{\text{Pt}} \cdot x_{\text{Pt,surface},r_i} \quad (19)$$

where  $x_{\text{Pt,surface},r_i}$  is the fraction of surface atoms of a Pt particle (of radius  $r_i$ ) over the total number of atoms. This is calculated based on a perfect FCC cubo-octahedral nanoparticle, as shown in ref [47] (Figure 2 therein). The mass of Pt oxide is:

$$M_{\text{Pt,surface oxide}} = M_{\text{Pt,surface}} \times 0.3 \quad (20)$$

Using the results of Pt particle size analysis in Figure 11 (a, c) and Figure S15 (a, c), the fraction of  $M_{Pt, surface\ oxide}$  relative to the total Pt loading in the images is in the range of 6%-16%, which can be averaged to be ~10% of the total Pt loading. Therefore, with the addition of ~1% Pt mass loss due to the dissolution of Pt particles <0.4 nm, the total amount of Pt loss is in agreement with the 7-11% Pt loss analyzed from membrane precipitates (Figures 11a and S14a). This is summarized in a schematic diagram (Figure 13).

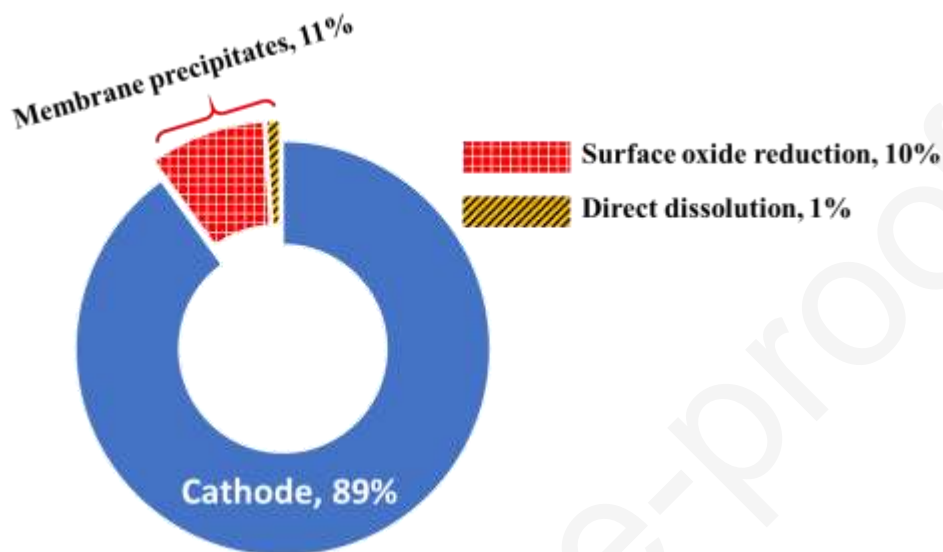


Figure 13. Schematic of Pt distribution in the cathode and the membrane region at end-of-test. Two sources of Pt dissolution are identified for the membrane precipitates.

With the loss of Pt quantified, it is possible to estimate the distribution of Pt and Ir across the CCM, which is shown in a schematic diagram (Figure 14). During electrolysis operation, iridium at the anode dissolves and migrates towards and through the membrane. A variety of Ir ionic species ranging from Ir (III), Ir (V), to Ir (VI) are produced as described in equations (1-7). Since the membranes adjacent to the anode are saturated with oxygen produced from the anode, Ir ions form the Ir oxide band as observed in Figure 4b. Other Ir ions further migrate to the cathode. They are either reduced by the crossover hydrogen and co-precipitated with Pt in the membrane, or re-deposited on the Pt catalyst at the cathode. Additionally, Pt surface oxide and Pt particles less than 0.4 nm diameter are dissolved during the transitional stage of the test and dissolved Pt ions migrate toward the membrane. Thus, Pt-Ir particles are formed and are mostly found in the half of the membrane that is close to the cathode. On the other hand, the anode suffered significant loss of Ir with only 30% remaining in the anode catalyst layer. The Ir band and membrane precipitates contain 10% and 18% of the initial Ir loading, respectively. The Ir deposition on the cathode contains 42% of the initial Ir loading, which is the majority of Ir that is lost. The loss of Pt is less significant than Ir with 10% dissolved and deposited in the membrane.



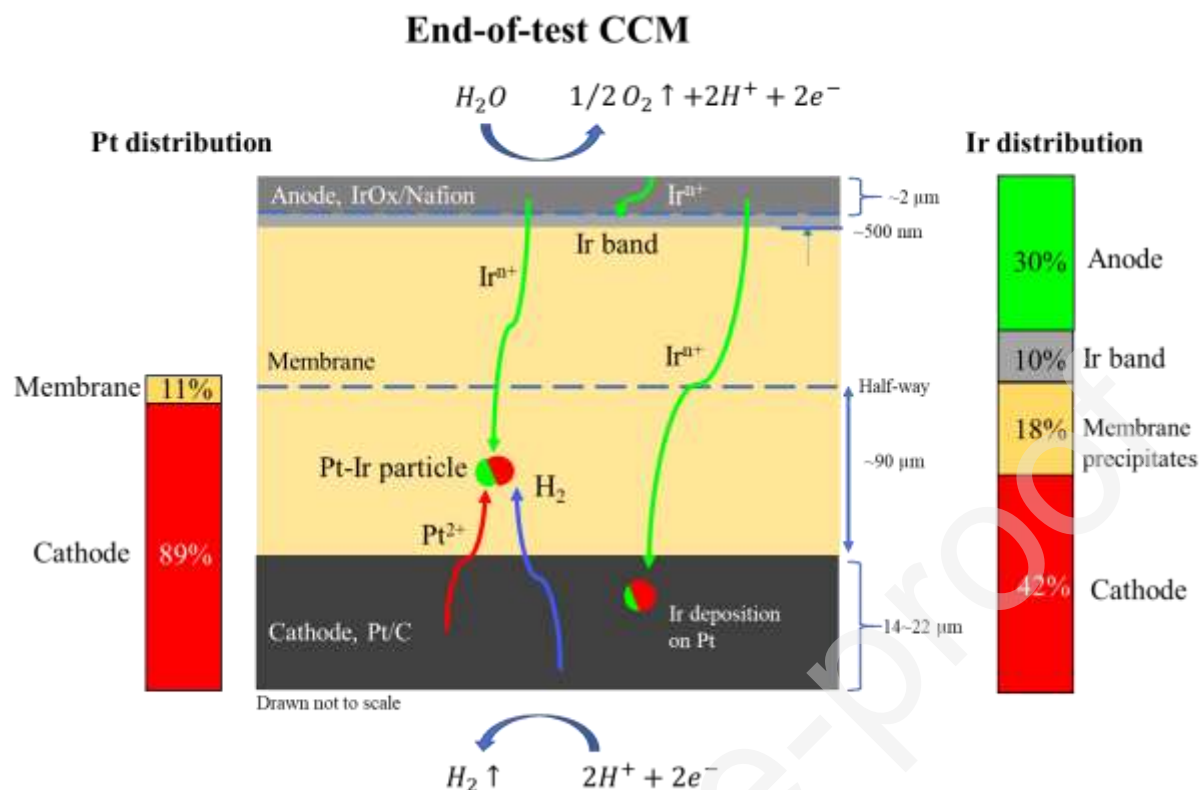


Figure 14. Schematic diagram depicting the mechanism leading to the formation of Pt-Ir precipitates and Ir band in the membrane. The distribution of Pt and Ir at different regions of the CCM is shown as weight percent. Ir<sup>n+</sup> is used to universally represent ionic Ir species.

## 4.0 Conclusions

Insights on the degradation mechanism of PEMWE CCM after long-term operation are provided using electron microscopy and chemical analysis. Major observations of the present study are:

- 1) Iridium dissolves in the anode during MEA tests with only 30% remaining at EOT. The dissolved iridium ions migrate through the membrane toward the cathode, forming an Ir oxide band at the anode/membrane interface and re-depositing as metallic Ir on the cathode catalyst. The Pt coating in the Ti PTL does not show significant Pt dissolution and migration. At a minimum, the amount of Pt dissolved is not identifiable from XEDS analysis.
- 2) The Pt catalysts on the cathode show iridium re-deposition on the surface as well as Pt dissolution. The Pt dissolution comes from Pt particles that are less than 0.4 nm in diameter at BOT and the reduction of Pt surface oxide in the initial transient stage of MEA testing. This leads to increased Pt ion concentration that can move toward the membrane by diffusion.
- 3) The membrane shows significant loss of mechanical integrity at EOT. Pt-Ir metallic precipitates (5-10 nm) are found in the half of membrane close to cathode where Pt and Ir ions meet and reduced by crossover hydrogen. In the case of low catalyst loadings, the size and density of Pt-Ir precipitates are much smaller than that of the precipitates formed with high Ir and Pt loaded electrodes.
- 4) For the first time, the mechanism of cathode dissolution is proposed using established physical models of direct Pt dissolution from small particles and Pt dissolution during rapid oxide reduction during the initial transient state of MEA testing. These lead to the formation of Pt-Ir precipitates in the membrane.



- 5) It is noted that the catalyst layer under the sealing surface still suffers some degree of degradation, although no Ir band is observed. Ir is found in the membrane adjacent to cathode and in the cathode layer within 1  $\mu\text{m}$  from the cathode/membrane interface, probably as the result of diffusion.
- 6) Finally, the distribution of Pt and Ir at EOT MEA is obtained with the estimate of Pt and Ir loss from each electrode. Iridium shows significant loss from the anode due to dissolution and migration.

It remains a challenge to determine the oxidation state of Pt and Ir in the EOT MEA with EELS due to interference from the strong plasmon signal in the spectrum overlapping with Pt and Ir peaks. Thus, the metallic phase of Pt-Ir precipitates and Ir deposits in the cathode are postulated with the oxygen distribution obtained in XEDS mapping.

## Conflicts of interest

There are no conflicts to declare.

## Acknowledgement

The authors would like to thank the University of Connecticut for funding of the electron microscopy work and the Department of Energy (DE-SE0009213) for financial support on catalyst development and testing. The authors would like to thank Thermo Fisher Scientific-Center for Advanced Material and Microscopic Analysis for providing electron microscopes. The authors would like to thank Dr. Nemanja Danilovic and Dr. Christopher Capuano at Nel Hydrogen for MEA testing. The authors would like to thank Marcia Reid and Dr. Natalie Hamada at McMaster University for preparing the ultramicrotome specimen and TEM-EELS analysis. The authors would also like to thank Dr. C Barry Carter for the HRSTEM imaging of the Pt catalysts (Figures 10 and S15).

## References

- [1] F.J. Vivas, A. De las Heras, F. Segura, J.M. Andújar, A review of energy management strategies for renewable hybrid energy systems with hydrogen backup, *Renewable and Sustainable Energy Reviews* 82 (2018) 126-155.
- [2] K. Bennaceur, B. Clark, M.J. Franklin, T.S. Ramakrishnan, C. Roulet, E. Stout, Hydrogen: A future energy carrier? *Oilfield Review* 17 (2005) 30-41.
- [3] K. Mazloomi, C. Gomes, Hydrogen as an energy carrier: Prospects and challenges, *Renewable and Sustainable Energy Reviews* 16 (2012) 3024-3033.
- [4] G. Cipriani, V. Di Dio, F. Genduso, D. La Cascia, R. Liga, R. Miceli, et al., Perspective on hydrogen energy carrier and its automotive applications, *International Journal of Hydrogen Energy* 39 (2014) 8482-8494.
- [5] S. Sharma, S.K. Ghoshal, Hydrogen the future transportation fuel: From production to applications, *Renewable and Sustainable Energy Reviews* 43 (2015) 1151-1158.
- [6] S.E. Hosseini, M.A. Wahid, Hydrogen production from renewable and sustainable energy resources: Promising green energy carrier for clean development, *Renewable and Sustainable Energy Reviews* 57 (2016) 850-866.

- [7] E.S. Hanley, J. Deane, B.Ó Gallachóir, The role of hydrogen in low carbon energy futures—A review of existing perspectives, *Renewable and Sustainable Energy Reviews* 82 (2018) 3027-3045.
- [8] A. Buttler, H. Spliethoff, Current status of water electrolysis for energy storage, grid balancing and sector coupling via power-to-gas and power-to-liquids: A review, *Renewable and Sustainable Energy Reviews* 82 (2018) 2440-2454.
- [9] R. Maric, H. Yu, in: Fedorenko Y. (Ed.), *Nanostructures in Energy Generation, Transmission and Storage*, IntechOpen, Rijeka, 2019,.
- [10] C. Spori, J.T.H. Kwan, A. Bonakdarpour, D.P. Wilkinson, P. Strasser, The Stability Challenges of Oxygen Evolving Catalysts: Towards a Common Fundamental Understanding and Mitigation of Catalyst Degradation, *Angew. Chem. Int. Ed.* 56 (2017) 5994-6021.
- [11] U. Babic, M. Suermann, F.N. Büchi, L. Gubler, T.J. Schmidt, Critical Review—Identifying Critical Gaps for Polymer Electrolyte Water Electrolysis Development, *Journal of The Electrochemical Society* 164 (2017) F387-F399.
- [12] Q. Feng, X. Yuan, G. Liu, B. Wei, Z. Zhang, H. Li, et al., A review of proton exchange membrane water electrolysis on degradation mechanisms and mitigation strategies, *Journal of Power Sources* 366 (2017) 33-55.
- [13] S. Siracusano, N. Van Dijk, R. Backhouse, L. Merlo, V. Baglio, A.S. Aricò, Degradation issues of PEM electrolysis MEAs, *Renewable Energy* 123 (2018) 52-57.
- [14] S. Sun, Z. Shao, H. Yu, G. Li, B. Yi, Investigations on degradation of the long-term proton exchange membrane water electrolysis stack, *Journal of Power Sources* 267 (2014) 515-520.
- [15] F. Fouda-Onana, M. Chandesris, V. Médeau, S. Chelghoum, D. Thoby, N. Guillet, Investigation on the degradation of MEAs for PEM water electrolyzers part I: Effects of testing conditions on MEA performances and membrane properties, *International Journal of Hydrogen Energy* 41 (2016) 16627-16636.
- [16] S. Siracusano, V. Baglio, N. Van Dijk, L. Merlo, A.S. Aricò, Enhanced performance and durability of low catalyst loading PEM water electrolyser based on a short-side chain perfluorosulfonic ionomer, *Applied Energy* 192 (2017) 477-489.
- [17] S. Siracusano, V. Baglio, S.A. Grigoriev, L. Merlo, V.N. Fateev, A.S. Aricò, The influence of iridium chemical oxidation state on the performance and durability of oxygen evolution catalysts in PEM electrolysis, *Journal of Power Sources* 366 (2017) 105-114.
- [18] M. Muto, M. Nagayama, K. Sasaki, A. Hayashi, Development and Evaluation of Ir Based Anode Electrocatalysts for Water Electrolysis, *ECS Transactions* 86 (2018) 719-726.
- [19] P. Lettenmeier, R. Wang, R. Abouatallah, S. Helmly, T. Morawietz, R. Hiesgen, et al., Durable Membrane Electrode Assemblies for Proton Exchange Membrane Electrolyzer Systems Operating at High Current Densities, *Electrochimica Acta* 210 (2016) 502-511.

- [20] S.A. Grigoriev, K.A. Dzhus, D.G. Bessarabov, P. Millet, Failure of PEM water electrolysis cells: Case study involving anode dissolution and membrane thinning, *International Journal of Hydrogen Energy* 39 (2014) 20440-20446.
- [21] S.A. Grigoriev, D.G. Bessarabov, V.N. Fateev, Degradation mechanisms of MEA characteristics during water electrolysis in solid polymer electrolyte cells, *Russian J. Electrochem.* 53 (2017) 318-323.
- [22] C. Rakousky, U. Reimer, K. Wippermann, M. Carmo, W. Lueke, D. Stolten, An analysis of degradation phenomena in polymer electrolyte membrane water electrolysis, *Journal of Power Sources* 326 (2016) 120-128.
- [23] C. Rakousky, U. Reimer, K. Wippermann, S. Kuhri, M. Carmo, W. Lueke, et al., Polymer electrolyte membrane water electrolysis: Restraining degradation in the presence of fluctuating power, *Journal of Power Sources* 342 (2017) 38-47.
- [24] C. Rakousky, G.P. Keeley, K. Wippermann, M. Carmo, D. Stolten, The stability challenge on the pathway to high-current-density polymer electrolyte membrane water electrolyzers, *Electrochimica Acta* 278 (2018) 324-331.
- [25] A.S. Gago, J. Bürkle, P. Lettenmeier, T. Morawietz, M. Handl, R. Hiesgen, et al., Degradation of Proton Exchange Membrane (PEM) Electrolysis: The Influence of Current Density, *ECS Transactions* 86 (2018) 695-700.
- [26] P. Paciok, M. Schalenbach, M. Carmo, D. Stolten, On the mobility of carbon-supported platinum nanoparticles towards unveiling cathode degradation in water electrolysis, *Journal of Power Sources* 365 (2017) 53-60.
- [27] S. Cherevko, S. Geiger, O. Kasian, A. Mingers, K.J.J. Mayrhofer, Oxygen evolution activity and stability of iridium in acidic media. Part 1. – Metallic iridium, *Journal of Electroanalytical Chemistry* 773 (2016) 69-78.
- [28] O. Kasian, J.-P. Grote, S. Geiger, S. Cherevko, K. J. J. Mayrhofer, The Common Intermediates of Oxygen Evolution and Dissolution Reactions during Water Electrolysis on Iridium, *Angew. Chem. Int. Ed.* 57 (2018) 2488-2491.
- [29] D.N. Buckley, L.D. Burke, The oxygen electrode. Part 6.-Oxygen evolution and corrosion at iridium anodes, *J. Chem. Soc. , Faraday Trans. 1* 72 (1976) 2431-2440.
- [30] S. Geiger, O. Kasian, B.R. Shrestha, A.M. Mingers, K.J.J. Mayrhofer, S. Cherevko, Activity and Stability of Electrochemically and Thermally Treated Iridium for the Oxygen Evolution Reaction, *Journal of The Electrochemical Society* 163 (2016) F3132-F3138.
- [31] S. Cherevko, S. Geiger, O. Kasian, A. Mingers, K.J.J. Mayrhofer, Oxygen evolution activity and stability of iridium in acidic media. Part 2. – Electrochemically grown hydrous iridium oxide, *Journal of Electroanalytical Chemistry* 774 (2016) 102-110.
- [32] S. Cherevko, T. Reier, A.R. Zeradjanin, Z. Pawolek, P. Strasser, K.J.J. Mayrhofer, Stability of nanostructured iridium oxide electrocatalysts during oxygen evolution reaction in acidic environment, *Electrochemistry Communications* 48 (2014) 81-85.

- [33] S. Siracusano, N. Hodnik, P. Jovanovic, F. Ruiz-Zepeda, M. Šala, V. Baglio, et al., New insights into the stability of a high performance nanostructured catalyst for sustainable water electrolysis, *Nano Energy* 40 (2017) 618-632.
- [34] N. Briguglio, S. Siracusano, G. Bonura, D. Sebastián, A.S. Aricò, Flammability reduction in a pressurised water electrolyser based on a thin polymer electrolyte membrane through a Pt-alloy catalytic approach, *Applied Catalysis B: Environmental* 246 (2019) 254-265.
- [35] C. Rozain, E. Mayousse, N. Guillet, P. Millet, Influence of iridium oxide loadings on the performance of PEM water electrolysis cells: Part II-Advanced oxygen electrodes, *Applied Catalysis B: Environmental* 182 (2016) 123-131.
- [36] M.K. Debe, S.M. Hendricks, G.D. Vernstrom, M. Meyers, M. Brostrom, M. Stephens, et al., Initial Performance and Durability of Ultra-Low Loaded NSTF Electrodes for PEM Electrolyzers, *Journal of The Electrochemical Society* 159 (2012) K165-K176.
- [37] K.E. Ayers, J.N. Renner, N. Danilovic, J.X. Wang, Y. Zhang, R. Maric, et al., Pathways to ultra-low platinum group metal catalyst loading in proton exchange membrane electrolyzers, *Catalysis Today* 262 (2016) 121-132.
- [38] H. Yu, N. Danilovic, Y. Wang, W. Willis, A. Poozhikunnath, L. Bonville, et al., Nano-size IrOx catalyst of high activity and stability in PEM water electrolyzer with ultra-low iridium loading, *Applied Catalysis B: Environmental* 239 (2018) 133-146.
- [39] H. Yu, A. Baricci, A. Casalegno, L. Guetaz, L. Bonville, R. Maric, Strategies to mitigate Pt dissolution in low Pt loading proton exchange membrane fuel cell: II. A gradient Pt loading design, *Electrochimica Acta* 247 (2017) 1169-1179.
- [40] H. Yu, A. Baricci, A. Bisello, A. Casalegno, L. Guetaz, L. Bonville, et al., Strategies to mitigate Pt dissolution in low Pt loading proton exchange membrane fuel cell: I. A gradient Pt particle size design, *Electrochimica Acta* 247 (2017) 1155-1168.
- [41] P.J. Ferreira, G.J. la O', Y. Shao-Horn, D. Morgan, R. Makharia, S. Kocha, et al., Instability of Pt/C Electrocatalysts in Proton Exchange Membrane Fuel Cells: A Mechanistic Investigation, *J. Electrochem. Soc.* 152 (2005) A2256-A2271.
- [42] S. Cherevko, N. Kulyk, K.J.J. Mayrhofer, Durability of platinum-based fuel cell electrocatalysts: Dissolution of bulk and nanoscale platinum, *Nano Energy* 29 (2016) 275-298.
- [43] L. Tang, X. Li, R.C. Cammarata, C. Friesen, K. Sieradzki, Electrochemical Stability of Elemental Metal Nanoparticles, *J. Am. Chem. Soc.* 132 (2010) 11722-11726.
- [44] L. Tang, B. Han, K. Persson, C. Friesen, T. He, K. Sieradzki, et al., Electrochemical Stability of Nanometer-Scale Pt Particles in Acidic Environments, *J. Am. Chem. Soc.* 132 (2010) 596-600.
- [45] W.J. Plieth, Electrochemical properties of small clusters of metal atoms and their role in the surface enhanced Raman scattering, *J. Phys. Chem.* 86 (1982) 3166-3170.

[46] J.M. Roller, M.J. Arellano-Jiménez, H. Yu, R. Jain, C.B. Carter, R. Maric, Catalyst nanoscale assembly from the vapor phase on corrosion resistant supports, *Electrochim. Acta* 107 (2013) 632-655.

[47] G. Wang, M.A. Van Hove, P.N. Ross, M.I. Baskes, Quantitative prediction of surface segregation in bimetallic Pt–M alloy nanoparticles (M=Ni,Re,Mo), *Progress in Surface Science* 79 (2005) 28-45.